Chemistry & Biology
Article

Crystal Structures of Lipoglycopeptide Antibiotic Deacetylases: Implications for the Biosynthesis of A40926 and Teicoplanin

Yaozhong Zou,[1] Joseph S. Brunzelle,[2] and Satish K. Nair[1,3,4,*]
[1]Department of Biochemistry, University of Illinois at Urbana-Champaign, 600 S. Mathews Avenue, Urbana, IL 61801, USA
[2]Life Sciences Collaborative Access Team, Northwestern University, Argonne, IL 60439, USA
[3]Center for Biophysics and Computational Biology
[4]Institute for Genomic Biology
University of Illinois at Urbana-Champaign, 600 S. Mathews Avenue, Urbana, IL 61801, USA
*Correspondence: snair@uiuc.edu
DOI 10.1016/j.chembiol.2008.05.009

SUMMARY

The lipoglycopeptide antibiotics teicoplanin and A40926 have proven efficacy against Gram-positive pathogens. These drugs are distinguished from glycopeptide antibiotics by *N*-linked long chain acyl-D-glucosamine decorations that contribute to antibacterial efficacy. During the biosynthesis of lipoglycopeptides, tailoring glycosyltransferases attach an *N*-acetyl-D-glucosamine to the aglycone, and this *N*-acetyl-glucosaminyl pseudoaglycone is deacetylated prior to long chain hydrocarbon attachment. Here we present several high-resolution crystal structures of the pseudoaglycone deacetylases from the biosynthetic pathways of teicoplanin and A40926. The cocrystal structure of the teicoplanin pseudoaglycone deacetylase with a fatty acid product provides further insights into the roles of active-site residues, and suggests mechanistic similarities with structurally distinct zinc deacetylases, such as peptidoglycan deacetylase and LpxC. A unique, structurally mobile capping lid, located at the apex of these pseudoaglycone deacetylases, likely serves as a determinant of substrate specificity.

INTRODUCTION

As the prevalence of antibiotic-resistant bacteria continues to become a global health concern, the search for novel antimicrobials with broad-spectrum efficacy and low toxicity remains a critical challenge for the biomedical community (Martinez et al., 2007; Zinner, 2007). The glycopeptide antibiotic vancomycin **1** (Figure 1) (trade names: Vancocyn, Lyphocin) has proven effective for treatment against infections from resistant, Gram-positive pathogens (Moellering, 2006), including methicillin-resistant *Staphylococcus aureus* (MRSA) (Anstead and Owens, 2004; Anstead et al., 2007) and drug-resistant pneumococci (Cunha, 2006). However, the emergence of vancomycin-resistant bacteria, including vancomycin-resistant enterococci (Murray, 2000) and vancomycin-intermediate and -resistant *S. aureus* (VISA and VRSA, respectively) (Hiramatsu et al., 1997; Sieradzki et al., 1999), threatens this last line of defense against fatal infections. The lipoglycopeptide antibiotics teicoplanin **2** (trade name: Targocid) (Spencer and Bryson, 1995) and A40926 **4** (a derivative of which is trademarked as Dalbavancin) (Scheinfeld, 2007) have demonstrated minimal toxicity, and proven efficacy against Gram-positive MRSA and VRSA (Van Bambeke, 2006). These lipoglycopeptides exert their antimicrobial effect in a manner similar to glycopeptides, such as vancomycin, by targeting the *N*-acyl-D-Ala-D-Ala peptides of peptidoglycan precursors to inhibit cell wall synthesis in Gram-positive bacteria (Kahne et al., 2005).

Like the glycopeptide vancomycin, the lipoglycopeptides teicoplanin and A40926 are composed of a heptapeptide aglycone that is further decorated with carbohydrates (Donadio et al., 2005). Unlike vancomycin, a characteristic modification found only in lipoglycopeptides is the attachment of an *N*-acyl-D-glucosamine at position 4 of the heptapeptide aglycone (Goldstein et al., 1987; Malabarba et al., 1984). Although the heptapeptide core is thought to be sufficient to target the *N*-acyl-D-Ala-D-Ala di-peptide, the carbohydrate and acyl groups contribute greatly to the antimicrobial efficacy of lipoglycopeptides (Beauregard et al., 1995; Wiliams and Bardsley, 1999). In particular, the hydrophobic acyl chain of the *N*-acyl-D-glucosamine can anchor the antibiotic at the cell membrane, thereby increasing the local antibiotic concentration at the target site for its activity (Cooper and Williams, 1999). The increased efficacy of teicoplanin against vancomycin-resistant enterococci has been directly attributed to the hydrophobic acyl chain (Dong et al., 2002), prompting research efforts toward the design of alkyl derivatives of glycopeptides with increased antimicrobial properties relative to the parent compounds. The success of this approach is reflected in the fact that telavancin **5**, a semisynthetic derivative of vancomycin that contains a decylaminoethyl appendage (Higgins et al., 2005), and oritavancin **6**, a *N*-alkyl-*p*-chlorophenylbenzyl derivative of chloroeremomycin (Allen and Nicas, 2003), are both currently in phase III clinical trials for use against Gram-positive infections. Hence, semisynthetic and genetic approaches toward *N*-acyl modification of glycopeptides are of significant pharmaceutical interest.

The elucidation of the biosynthetic routes for lipoglycopeptide production by actinomycetes have established the general

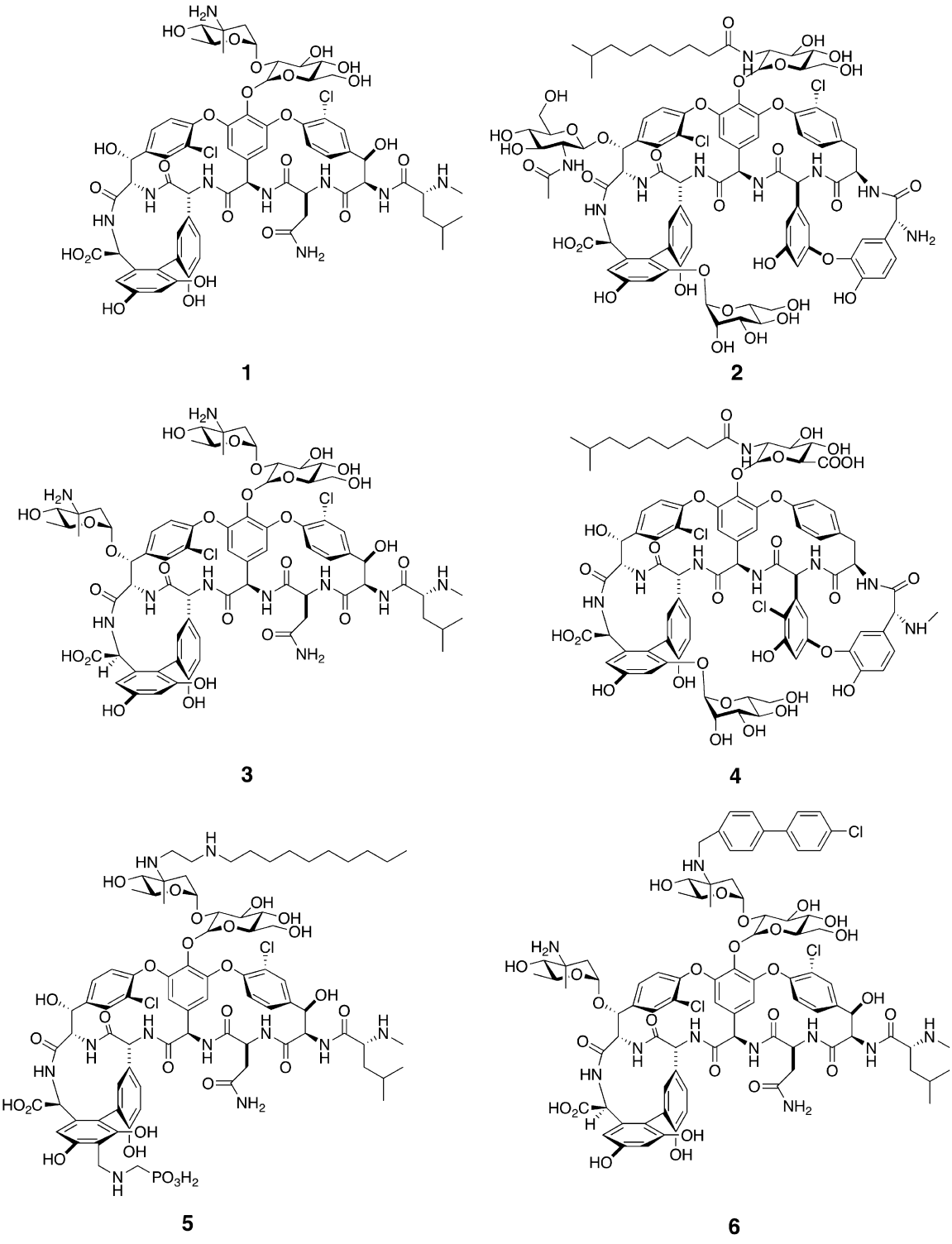

Figure 1. Chemical Structures of the Glycopeptide Antibiotics

The structures of vancomycin (**1**) and chloroeremomycin (**3**); the lipoglycopeptides teicoplanin (**2**; shows the A_2-5 teicoplanin) and A40926 (**4**); and two semisynthetic lipoglycopeptide antibiotics that are currently in clinical trials telavancin (**5**) and oritavancin (**6**).

scheme for *N*-acyl-D-glucosamine tailoring of the aglycone for both teicoplanin in *Actinoplanes teichomyceticus* (Li et al., 2004; Sosio et al., 2004) and A40926 in *Nonomuraea* sp. ATCC 39727 (Sosio et al., 2003). Specifically, the addition of a glucosamine moiety to the hydroxyl group of amino acid 4 by a glycosyltransferase (Dbv9 for A40926, and Orf10* for teicoplanin) is

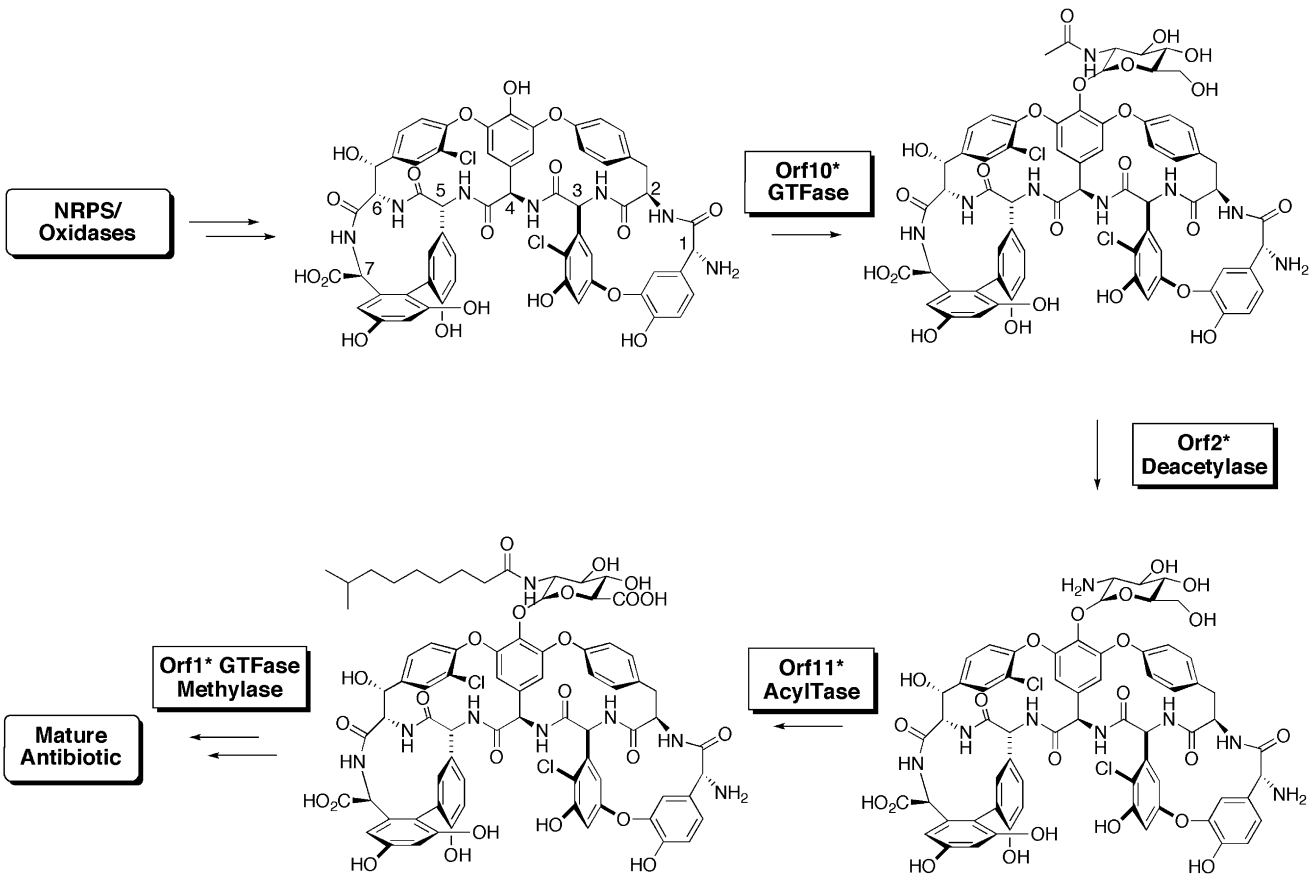

Figure 2. Schematic Illustration of the Steps Involved in the Biosynthesis of Lipoglycopeptide Antibiotics

The linear heptapeptide backbone is synthesized by the nonribosomal peptide synthases (NRPS) and crosslinked by oxidases to yield the core aglycone structure. A tailoring glycosyltransferase adds *N*-acetyl-D-glucosamine to amino acid 4, followed by deacetylation by a pseudoaglycone deacetylase prior to acylation to yield an *N*-acyl-D-glucosamine. Additional tailoring steps are carried out by methylases and an additional glycosyltransferase to yield the mature antibiotic.

followed by *N*-acylation at the glucosamine by an acyltransferase (Orf8 for A40926, and Orf11* for teicoplanin) (Kruger et al., 2005; Li et al., 2004; Sosio et al., 2003; Figure 2). The glycosyltransferases involved are shown to have broad specificity, and can utilize either an amino sugar (UDP-D-glucosamine) or an activated amino sugar (UDP-*N*-acetyl-D-glucosamine) as a substrate, in vitro (Kruger et al., 2005; Li et al., 2004). However, as bacteria cannot produce UDP-D-glucosamine as a primary metabolite, the in vivo substrate for the Orf10* glycosyltransferase was established as UDP-*N*-acetyl-D-glucosamine (Li et al., 2004). Prior to acylation by Orf11*, the *N*-acetyl-glucosaminyl pseudoaglycone must be deacetylated to yield a free 2′-amine (Figure 2). Bioinformatic analysis identifies putative deacetylase genes within the biosynthetic gene clusters for lipoglycopeptide antibiotics, and the gene products Orf2* and Dbv21 are shown to encode pseudoaglycone deacetylases for the maturation of tecioplanin and A40926, respectively (Ho et al., 2006; Truman et al., 2006). Homologs of these proteins are also encoded in the biosynthetic gene cluster for the aminoglycoside antibiotic, butirosin, as the BtrD gene product, which was initially reported to harbor nucleotidyltransferase activity, has more recently been functionally reclassified as a homolog of the pseudoaglycone deacetylases (Truman et al., 2007).

The pseudoaglycone deacetylases Orf2* and Dbv21 are roughly the same molecular mass (roughly 30,000 Da) and share 65% sequence identity with each other. Biochemical in vitro activity has been established for recombinant forms of both Orf2* (deacetylation of *N*-acetyl-D-glucosaminyl teicoplanin pseudoaglycone) and Dbv21 (deacetylation of *N* -acetyl-D-glucosaminyl A40926 pseudoaglycone) (Ho et al., 2006; Truman et al., 2006). The two enzymes show moderate promiscuity for substrate, and Dbv21 can also accept *N*-acetyl-D-glucosaminyl teicoplanin pseudoaglycone (but not teicoplanin) as a substrate. Interestingly, Orf2* cannot accept *N*-acetyl-D-glucosamine or *N*-acetyl-D-glucosamine-UDP as substrate, which suggests that the teicoplanin aglycone is important for substrate recognition (Ho et al., 2006; Truman et al., 2006). Finally, Orf2* is also capable of removing the acyl group from mature teicoplanin to yield a precursor with a free 2′-amine, which can then be regio-specifically modified for the production of novel glycopeptide antibiotics (Truman et al., 2006).

The pseudoaglycone deacetylases share modest sequence and functional similarities with MshB, a zinc-dependent metalloprotein that deacetylates *N*-acetyl-D-myo-inosityl-2-deoxy-α-D-glucopyranoside during the production of mycothiol in actinomycetes (Newton et al., 2000, 2006; Rawat et al., 2003). The crystal

structure of MshB reveals a structural similarity to the glycogen phosphorylase/glycosyl transferase superfamily of protein folds (Maynes et al., 2003; McCarthy et al., 2004). A single zinc ion is located at the active site, where it is coordinated by protein residues His-13, Asp-16, and His-147, with two water molecules completing a square pyramidal coordination geometry. Binding of substrate is thought to displace the first water molecule, and the second metal-activated water (or hydroxide) serves as the nucleophile for the hydrolysis reaction. Residues that flank the metal binding site are implicated to act as a general base or to stabilize the tetrahedral intermediate during hydrolysis (Maynes et al., 2003; McCarthy et al., 2004).

The structure of MshB does not serve as a valid template for understanding the mechanism of the pseudoaglycone deacetylases. Although the 30% sequence identity likely indicates a common topology, distinct features of the active site cannot be successfully predicted due to the low sequence similarity shared between these proteins. Additionally, although divalent metal ions are critical to the function of Orf2*, the identity of the metal has not been determined, as different divalent ions only show slight difference in catalytic efficiency. In addition, the presence of high concentrations of divalent zinc is inhibitory to deacetylase activity, consistent with similar effects previously observed for zinc-dependent metalloproteases (Truman et al., 2006). However, the mechanism for zinc inhibition of the pseudoaglycone deacetylases has yet to be established.

In order to provide a molecular framework for understanding the mechanism of these enzymes, we present several high-resolution crystal structures of pseudoaglycone deacetylases. We have determined the structure of the teicoplanin deacetylase Orf2* to 1.6 Å resolution, and the A40926 deacetylase Dbv21 to 2.1 Å resolution. In order to elucidate the binding site for the lipoglycopeptide long chain fatty acid, we have determined the 2.1 Å resolution cocrystal structure of Orf2* bound to a product decanoic acid. In order to understand the molecular basis for Zn^{2+} inhibition of Orf2*, we present the structure of Orf2* bound to excess zinc. Our structures complement previous biochemical data to provide a molecular understanding of the mechanism of these pseudoaglycone deacetylase structures, and will be essential in biotransformation applications for developing novel lipoglycopeptide antibiotics.

RESULTS AND DISCUSSION

Overall Structure

The crystal structure of the teicoplanin deactylase Orf2* was determined to 1.6 Å resolution with single-wavelength anomalous scattering from crystals grown from selenomethionine incorporated protein. Residues Thr-8 through Ser-273 (out of a total of 273 residues) could be modeled without any interruptions, and the structure has been refined to an R factor/free R factor of 19.4%/22.3% (Figure 3A). The structure of the A40926 deacetylase Dbv21 was determined to 2.1 Å resolution by molecular replacement with the refined coordinates of Orf2* as a search probe (Figure 3B). The first six amino acids of the protein and an internal loop consisting of residues 102–124 have not been modeled due to disorder. The structure has been refined to an R factor/free R factor of 20.9%/25.2% (see Table 1 for relevant phasing and refinement statistics).

The overall structures of Orf2* and Dbv21 are similar, as expected from the 65% sequence similarity shared between the two proteins (Figure 3C). The root-mean-square deviation (rmsd) between the polypeptides is 1.2 Å over 240 aligned main chain atoms. The overall folds of the two pseudoaglycone deacetylases consist of a single α/β domain with large loops that interconnect the secondary structure elements. Prior studies have established that Orf2* can deacetylate teicoplanin (Truman et al., 2006), suggesting that the acyl chain of the mature antibiotic can be accommodated in a hydrophobic pocket. Detailed structural comparisons of Orf2* and Dbv21 in the vicinity of the active site are restrictive, as a loop that caps the active site is disordered in the structure of the latter enzyme (see below for details).

A structure-based similarity search of Orf2* with a Dali (Holm and Sander, 1995) search engine queried against the Protein Data Bank (Berman et al., 2000) identifies MshB as the closest structural homolog (Z score = 18.3; rmsd = 2.7 Å over 194 aligned residues) (Maynes et al., 2003; McCarthy et al., 2004). Modest structural similarity is also noted with various glycosyltransferases and other proteins of the glycogen phosphorylase/glycosyl transferase (GPGTF) superfamily of folds (Liu and Mushegian, 2003). The closest structural homologs of the pseudoaglycone deacetylases also utilize substrates that contain a substituted *N*-acetyl-D-glucosamine, suggesting a common evolutionary ancestry of the active-site structural elements. Although the core topological elements are similar between the pseudoaglycone deacetylases, MshB, and glycosyltransferases of the GPGTF superfamily, only the pseudoaglycone deacetylases and MshB are single-domain metalloproteins containing a substrate binding site that flanks the zinc ion. In contrast, members of the GPGTF superfamily contain a tandem repeat of this architecture, do not contain any metal ions, and harbor a substrate binding site at the interdomain cleft.

Active-Site Architecture

In the structures of each of the pseudoaglycone deacetylases, a single divalent metal ion is situated at the base of a 16 Å cavity near the center of the molecule (Figures 3A and 3B). The metal is coordinated by protein residues His-16 (Zn^{2+}–Nδ1, distance = 2.09 Å), Asp-19 (Zn^{2+}–Oδ2, distance = 2.12 Å), and His-164 (Zn^{2+}–Nε1, distance = 2.14 Å) (Orf2* numbering) (Figure 4A). The identity of the metal is confirmed to be zinc based on metal analysis, and results from X-ray fluorescence scans. Anomalous difference Fourier maps, calculated with phases from the final refined model (minus all metal atoms), and coefficients from Bijvoet differences from data collected at the zinc absorption edge (λ = 1.27819 Å), shows significant spherical density at the zinc binding site (Figure 4B). Additionally, the coordination geometry of the metal is similar to that observed for zinc ions in other metalloenzymes. Two solvent molecules (distances from Zn^{2+} of 2.00 and 2.11 Å) complete the coordination sphere to yield a square pyramidal coordination geometry for the zinc ion (Figure 4C). The disposition of the metal ion deep within the active site cavity explains why the addition of a large chelator EDTA had minimal affect on enzyme activity (Truman et al., 2006).

Adjacent to the active site, a stretch of continuous electron density, which has been interpreted as a polyethylene glycol

 ©2008 Elsevier Ltd All rights reserved

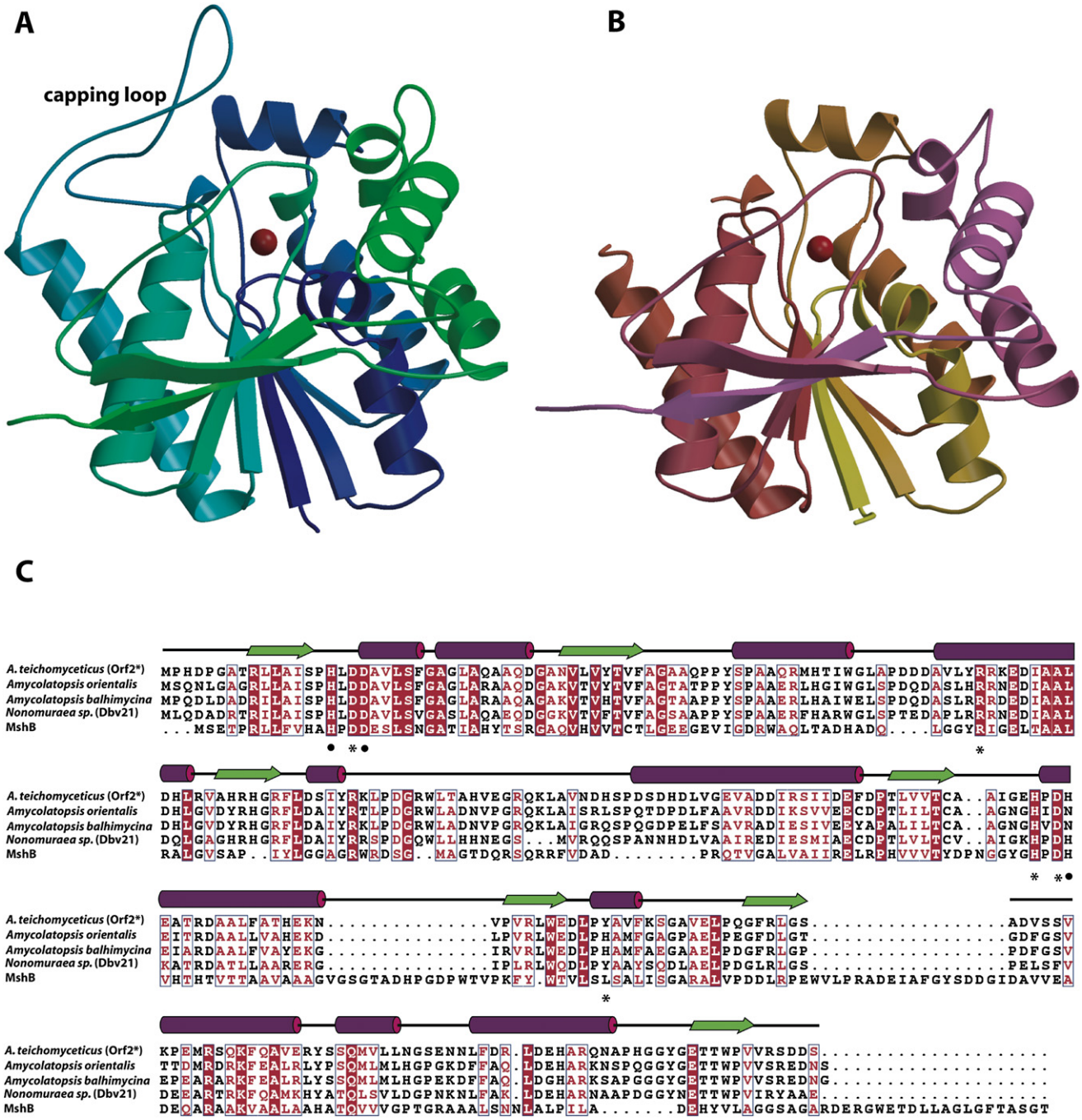

Figure 3. Structures of Pseudoaglycone Deacetylases Orf2* and Dbv21

(A) Ribbon diagram derived from the 1.6 Å resolution structure of the teicoplanin pseudoaglycone deacetylase Orf2* shown in a color ramp from blue to green. The catalytically requisite zinc ion is shown as a red sphere and the location of the capping loop is noted.

(B) Ribbon diagram derived from the 2.1 Å resolution structure of the A40926 pseudoaglycone deactylase Dbv21 shown in a color ramp from yellow to purple. Electron density for the capping loop is ill defined, and residues 102–124 have not been modeled due to disorder.

(C) Structure-based sequence alignment of enzymes related to the pseudoaglycone deactylases. Note that, while the gene clusters for the biosynthesis of balhimycin (*A. balhimycina*) and chloroeremomycin (*A. orientalis*) encode for gene products with 60% sequence identity, neither antibiotic contains a glucosaminyl group. In addition, the gene product from *A. orientalis* is shown to harbor nucleotidyltransferase activity.

heptamer, occupies the hydrophobic acyl chain binding pocket (Figure 4A). Additional protein residues near the metal center include Asp-18, His-161, Asp-163, and Tyr-190 (Figure 4A). By analogy to chemically similar residues that are found near the active sites of other zinc-dependent deacetylases, Asp-18 is the general base that activates one of the zinc-bound

Table 1. Data Collection, Phasing, and Refinement Statistics

	SeMet Orf2*	Orf2*-Zinc	Orf2*-Decanoate	Dbv21
Data collection				
Space group	$P2_1$	$P2_1$	$P2_1$	$P4_12_12$
Cell dimensions				
a, *b*, *c* (Å)	42.2, 64.3, 50.5	41.3, 64.3, 49.9	41.7, 64.5, 50.5	62.9 62.9 159.9
α, β, γ (°)	90.0, 99.2, 90.0	90.0, 98.9, 90.0	90.0, 98.9, 90.0	90.0, 90.0, 90.0
Resolution (Å)	50.0–1.6 (1.67–1.60)[a]	50–2.0 (2.07–2.0)[a]	50–1.8 (1.86–1.8)[a]	50–2.07 (2.15–2.07)[a]
R_{sym} (%)[b]	4.3 (28.8)	4.4 (21.8)	4.6 (10.6)	8.5 (68.2)
I/σ(I)	34.5 (4.8)	33.6 (5.3)	23.8 (9.2)	15.9 (3.1)
Completeness (%)	98.4 (94.3)	99.3 (93.5)	97.3 (92.2)	96.5 (85.3)
Redundancy	4.2 (4.1)	4.0 (3.2)	2.8 (2.5)	8.7 (5.5)
$\|F_H\|$/e (acentric)	1.67			
FOM/DM FOM[c]	0.37/0.90			
Refinement				
Resolution (Å)	25.0–1.6	25.0–2.0	25.0–1.8	25.0–2.1
No. of reflections	32,604	16,079	22,587	18,476
R_{work}/R_{free} (%/%)[d]	19.4/22.4	19.8/24.1	17.6/22.0	20.9/25.2
No. of atoms				
Protein	2103	2074	2074	1865
Solvent	241	87	251	94
Zinc ion	1	5	1	1
Ligand			12	
Mean B value (Å^2)				
Protein	25.1	37.5	27.5	52.4
Solvent	37.7	39.0	41.4	52.7
Zinc ion	18.5	44.4	23.9	45.9
Ligand	—	—	39.8	—
Rmsd				
Bond lengths (Å)	1.129	1.145	1.179	1.384
Bond angles (°)	0.009	0.009	0.009	0.014

Abbreviations: acentric, acentric reflections; e, residual lack of closure error; F_H, structure factor amplitude of the heavy atom derivative; FOM, figure of merit.

[a] Highest resolution shell is shown in parenthesis.

[b] $R_{sym} = \Sigma\ |I_i - < I_i >|\ \Sigma\ I_i$, where I_i = intensity of the *i*th reflection and $< I_i >$ = mean intensity.

[c] Mean figure of merit before and after density modification.

[d] R factor = $\Sigma\ (|F_{obs}| - k|F_{calc}|)/\Sigma\ |F_{obs}|$ and R_{free} is the R value for a test set of reflections consisting of a random 5% of the diffraction data not used in refinement.

water molecules for nucleophilic attack on the acetate, and His-161 and Tyr-190 act to stabilize the negative charge on the tetrahedral intermediate during catalysis. Interestingly, the electron density around Tyr-190 in the structures of both pseudoaglycone deacetylases suggests mobility, and two conformers of this residues can be readily modeled in the 1.6 Å resolution structure of unliganded Orf2*. Presumably, substrate binding orients and stabilizes one conformer of Tyr-190 for effective stabilization of the oxyanion intermediate. Based on its location in the vicinity of the other catalytic residues, and the presumed function of equivalent residues in other deacetylases, Asp-163 likely accepts a proton from the imidazolium of His-161 and orients this residue for effective stabilization of the tetrahedral oxyanion intermediate and its flanking transition states.

Identification of a Binding Site for the Hydrophobic Acyl Chain

Various attempts to obtain cocrystal structures of Orf2* with substrate teicoplanin pseudoaglycone have not been successful. Consistent with prior biochemical data (Truman et al., 2006), we observe that Orf2* can also accommodate mature teicoplanin as a substrate, and the catalytic efficiency for the removal of the acyl chain by Orf2* is much lower than for the deacetylation reaction. Unfortunately, attempts to produce cocrystals of Orf2* bound to deacylteicoplanin have also been unsuccessful. Since the hydrophobic acyl chain is a product of the deacylation reaction, we also attempted cocrystallization of Orf2* with various long chain fatty acids. We presume that the fatty acid would bind to the enzyme at the same location as the acyl chain substituent of substrate teicoplanin, as has been observed in crystal

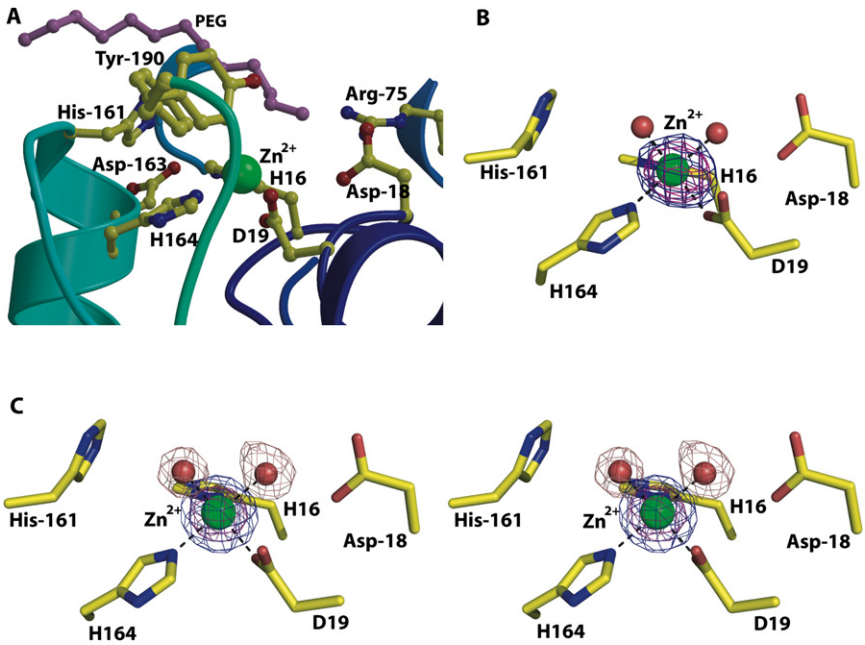

Figure 4. Close-Up View of the Active Site of Orf2*

(A) The zinc ion is shown in green, and catalytically relevant residues are shown as ball and stick models and labeled accordingly. Note that Tyr-190 occupies multiple conformations in the structure of the native enzyme. A molecule of polyethylene glycol (derived from the crystallization medium) occupied the hydrophobic binding site, and is shown in pink.

(B) Anomalous difference Fourier electron density map calculated with phases from the final refined model of Orf2* minus the metal atom and coefficients $|F^+| - |F^-|$, corresponding to Bijvoet differences from data collected at the zinc absorption edge (λ = 1.27819 Å). The contour levels are 4σ (blue mesh) and 8σ (purple mesh) above background.

(C) Stereo view of electron density maps calculated with Fourier coefficients $F_{obs} - F_{calc}$ with phases derived from the final refined model of unliganded Orf2* minus active-site features. The first map was calculated by omitting the coordinates of the zinc ion prior to one round of crystallographic refinement, and is contoured at 5σ (blue mesh) and 15σ (purple mesh). The second map was calculated by omitting the nonprotein zinc ligands, and is shown contoured at 3.5σ (salmon mesh). The final refined coordinates are superimposed with the zinc ion colored green, and the zinc-bound solvent molecules are colored red.

structures of other zinc-dependent deacetylases (Whittington et al., 2003). We were successful in obtaining the structure of Orf2* bound to decanoic acid to 1.8 Å resolution, and this structure has been refined to an R factor/free R factor of 17.6%/22.0% (see Table 1 for relevant refinement statistics).

The structure of the Orf2*-decanoic acid binary complex shows electron density adjacent to the zinc ion at the active site (Figure 5A). Although the density is somewhat discontinuous at the tail end of the hydrocarbon chain, the features are consistent with that of a bound decanoic acid ligand. In contrast to the binding mode of ligands observed in other cocrystal structures of other zinc-deacetylases, the carboxylate of the fatty acid does not engage the metal ion in a bidentate fashion. Rather, the electron density is consistent with one of the carbonyl oxygens displacing the presumptive nucleophilic water to engage in an inner-sphere coordination with zinc (zinc-oxygen distance = 2.16 Å). The second solvent molecule is not displaced (zinc-oxygen distance = 2.01 Å), and the pentacoordinate geometry at the metal is retained.

The hydrocarbon chain of the fatty acid is packed against one surface of the active-site cleft, where it engages in van der Waals interactions with hydrophobic residues Met-59, Trp-63, Ile-99, Leu-119, and Val-121 (Figure 5A). A number of polar residues can also be located along this cleft; most notably, Arg-75 and Asp-97. In the cocrystal structure of the related MshB deacetylase, a molecule of β-octylglucopyranoside is bound in the vicinity of equivalent residues, and this has been interpreted to suggest that these residues are involved in the recognition of the sugar moiety of the substrate. While Asp-97 may indeed play a role in sugar recognition, the location of Arg-75 is too distant to support a role in substrate recognition. By analogy to the mechanism of peptidoglycan deacetylase, the likely role of Arg-75 is to orient the general base Asp-18. Inferences on the role of this residue based on the MshB-β-octylglucopyranoside structure are difficult as: (1) the position of the bound β-octylglucopyranoside is not consistent between the two molecules of MshB in the crystallographic asymmetric unit of the cocrystal structure; (2) the structure in question lacks the catalytically requisite zinc ion, suggesting an unproductive binding mode for β-octylglucopyranoside; and (3) modeling of the sugar moiety of the teicoplanin pseudoaglycone onto the position of the β-octylglucopyranoside in the MshB cocrystal structure would not allow the acetyl group to be positioned in the vicinity of the zinc ion. Hence, Arg-75 is not directly involved in engaging the sugar moiety, and likely serves the other role of positioning the catalytic base.

Molecular Basis for Zinc Inhibition

In order to identify the requisite for a metal cofactor for pseudoaglycone deacetylase activity, the effects of various divalent metal ions on the activity of Orf2* were measured by Truman et al. (2006). The addition of a range of divalent metals has little effect on enzyme activity, suggesting either that the enzyme copurifies with a bound metal that is difficult to displace, or that enzyme activity is independent of metal cofactors. Addition of stoichiometric excess of zinc is shown to be inhibitory, and 3 mM total zinc ion completely abolishes deacetylase activity, as observed with several other zinc-dependent metalloenzymes. Hence, the lack of catalytic enhancement upon addition of exogenous divalent metal ions is likely a consequence of the fact that the catalytically requisite zinc ion is held tightly at the active site, is not disrupted during purification, and can not be disengaged by large chelating

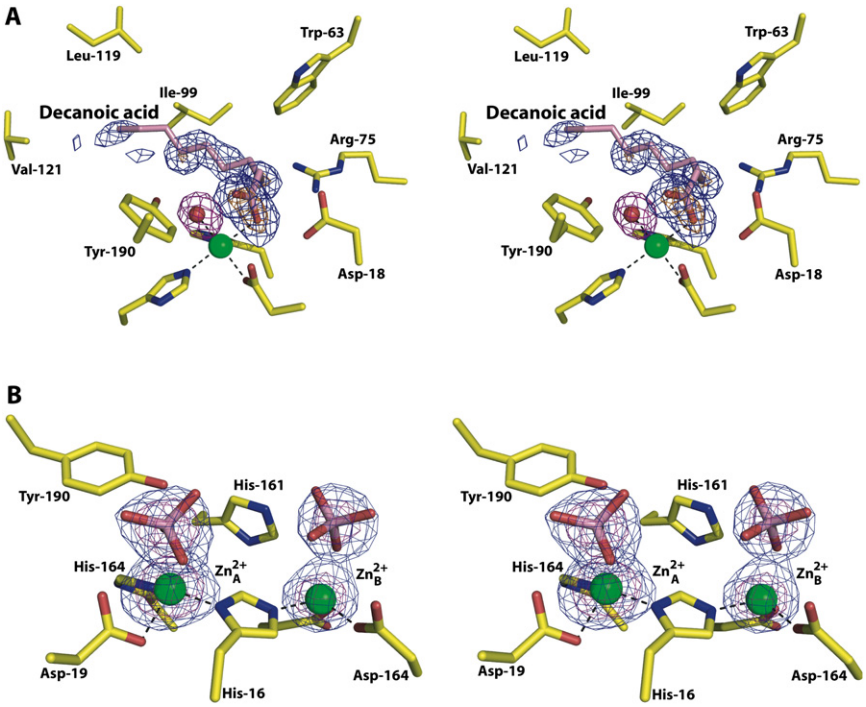

Figure 5. Close-Up Views of the Active Sites of the Orf2*-Decanoic Acid and Orf2*-Zinc Complexes

(A) Stereo view of electron density maps calculated with Fourier coefficients $F_{obs} - F_{calc}$ with phases derived from the refined 1.8 Å resolution structure of the Orf2*-decanoic acid complex. The first map was calculated with the coordinates for the fatty acid being omitted prior to one round of crystallographic refinement, and is contoured at 2.5σ (blue mesh) and 8σ (orange mesh). The second map was calculated by omitting the coordinates of the zinc-bound solvent molecule, and is contoured at 3σ (purple mesh). The final refined coordinates are superimposed, and the zinc ion is shown as a green sphere, the zinc-bound solvent as a red sphere, the fatty acid is shown with carbon atoms colored pink, and oxygen atoms are colored red.

(B) Stereo view of electron density maps calculated with Fourier coefficients $F_{obs} - F_{calc}$ with phases derived from the refined 2.0 Å resolution structure of the Orf2*-zinc complex. The map is calculated with the coordinates of the zinc ions and the nonprotein zinc ligands omitted prior to one round of crystallographic refinement, and is contoured at 4σ (blue mesh) and 10σ (purple mesh). The final refined coordinates of the complex are superimposed, with the zinc ion shown as a green sphere, the sulfate ion shown with the sulfur atoms colored pink, and the oxygen atoms colored red.

agents. In order to elucidate the molecular basis for zinc-mediated inhibition of the pseudoaglycone deacetylases, we determined the structure of Orf2* grown in the presence of 10 mM zinc sulfate to 2.0 Å resolution. The structure has been refined to an R factor/free R factor of 19.8%/24.1% (see Table 1 for relevant refinement statistics).

The structure reveals a number of electron-rich, spherical features in difference Fourier maps within the vicinity of the active site, which have been modeled as zinc ions (Figure 5B). The position and coordination geometry of the native zinc ion remains intact in the zinc-inhibited structure. However, the electron density at the nonprotein zinc ligand suggests that the zinc-bound solvent molecule has been replaced by a sulfate anion. Additionally, a second zinc ion is situated at a distance of 5.8 Å away from the native zinc, where it is coordinated by protein ligands His-16 (Zn^{2+}–Nε2, distance = 2.09 Å), Asp-97 (Zn^{2+}–Oδ1, distance = 1.94 Å), and Asp-163 (Zn^{2+}–Oδ2, distance = 1.84 Å), with another sulfate anion completing the coordination geometry. Both metals share a common ligand, with Nδ1 of His-16 coordinating to the native zinc and Nε2 of the same residue coordinating to the inhibitory metal. Such bridging coordination interactions with binuclear zinc centers are rare, and have only been previously observed in the structures of phosphorylcholine esterase (in which an aspartate bridges two zinc ions) (Hermoso et al., 2005) and superoxide dismutase (in which a histidine imidazolate bridges the zinc and copper ions) (Djinovic et al., 1992). The tetrahedral coordination of the inhibitory zinc ion at an alternate site is reminiscent of the binuclear zinc cluster observed in the structure of zinc-inhibited forms of zinc proteases (Gomez-Ortiz et al., 1997; Holland et al., 1995) and of the zinc-dependent UDP-(3-*O*-(*R*-3-hydroxymyristoyl))-*N*-acetylglucosamine deacetylase LpxC (Whittington et al., 2003). However, the 5.87 Å metal separation distance observed in the structure of zinc-inhibited Orf2* is significantly larger than the typical separation distances of 3.3 Å observed in other binuclear zinc clusters (Christianson, 1991). This larger separation observed in Orf2* is a consequence of the fact that a common coordinating residue (His-16) is interposed between the native and inhibitory binding sites.

By analogy to the mechanism of zinc inhibition of other zinc proteases and deacetylases, the mechanism of inhibition is likely due to steric exclusion of substrate from the active site. For example, the structure of the LpxC deacetylase bound to a substrate analog inhibitor TU-514 shows that the nitrogen atom of the hydroxamate occupies a location similar to that of the inhibitory zinc ion (Coggins et al., 2005; Gennadios et al., 2006). Likewise, the structure of zinc-inhibited thermolysin reveals that the inhibitory zinc occupies the presumed position of the carbonyl oxygen of the scissile peptide bond (Holland et al., 1995). In each of these structures, the inhibitory zinc ion is engaged by residues that facilitate catalysis by stabilizing the charge on the tetrahedral intermediate during catalysis. In the structure of zinc-inhibited Orf2*, active-site residue His-161 is situated adjacent to the inhibitory zinc ion, and this residue similarly acts as an electrostatic catalyst in pseudoaglycone deacetylation. Participation of Asp-97 in coordinating the inhibitory zinc ion is also consistent with the proposal that this residue participates in recognition of the sugar group of the pseudoaglycone.

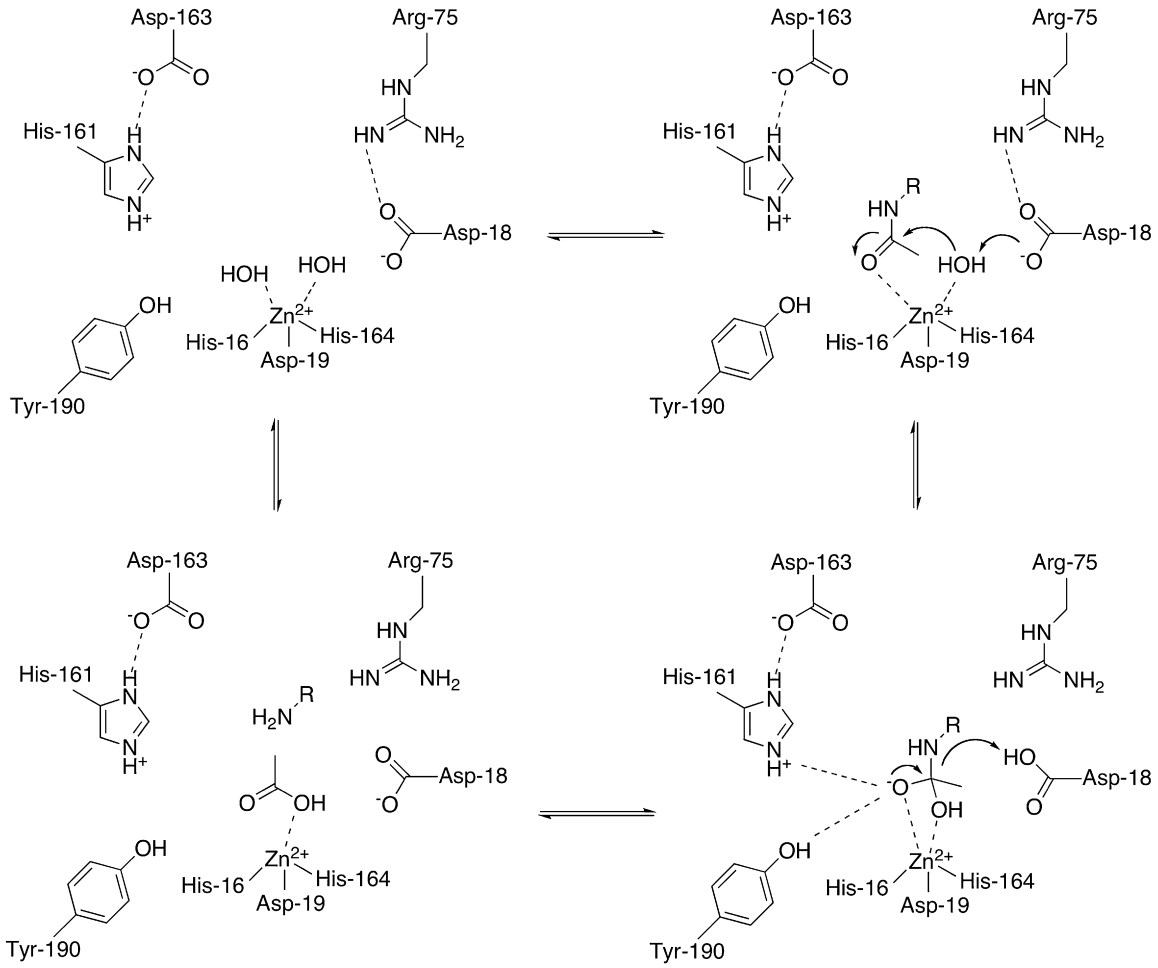

Figure 6. Proposed Catalytic Mechanism for Pseudoaglycone Deacetylation

The mechanistic proposal is based on inferences drawn from the crystallographic results presented here and by analogy to the proposed mechanisms for the mechanistically related, but structurally divergent, deacetylases LpxC and CE-4 family peptidoglycan deacetylase.

Proposed Catalytic Mechanism

The crystal structures of the pseudoaglycone deacetylases and their ligand complexes presented here suggest a mechanism consistent with those of other zinc-dependent deacetylases (Figure 6). In particular, a pentacoordinate zinc ion resides at the base of the active site, where it is ligated by enzyme residues His-16, Asp-19, and His-164, with two water molecules completing the coordination sphere. The carbonyl oxygen of the substrate displaces one of the two water ligands, and polarization of the oxygen atom of the carbonyl by the zinc activates the carbon atom for nucleophilic attack. The catalytic zinc ion also polarizes the second water molecule, promoting deprotonation by the general base Asp-18, and facilitating nucleophilic attack of this water at the scissile amide linkage of the substrate. Arg-75 orients and polarizes the carboxylate side chain of Asp-18 for its role as the catalytic base. The resulting tetrahedral oxyanion intermediate and the flanking transition states are stabilized by the zinc ion, the imidazolium of His-161, and by Tyr-190. Effective electrostatic catalysis by His-161 is provided by stabilization of the imidazolium by the carboxylate side chain of Asp-163. Asp-18 then serves as a proton donor to the leaving amino group to generate the reaction products.

One noteworthy distinction in the proposed deacetylation mechanism of the pseduoaglycone deacetylases concerns the role of Tyr-190 in oxyanion stabilization. Tyr-190 is not conserved between the pseudoaglycone deacetylases and the structurally related zinc deacetylase MshB. However, the three-dimensional structures of MshB show an equivalent tyrosine residue situated in a similar position (Maynes et al., 2003; McCarthy et al., 2004). In particular, the α helix that harbors Tyr-190 is deleted in MshB, but a tyrosine residue (Tyr-142) located at the apex of a neighboring α helix is oriented in a conformation similar to that of Tyr-190 in Orf2*. In the crystal structure of the structurally distinct *Streptococcus pneumoniae* peptidoglycan deacetylase (Blair et al., 2005), a tyrosine residue, Tyr-367, is situated proximally to the supposed location of the oxyanion of the tetrahedral intermediate. Mutation of this residue to alanine impairs catalytic activity, suggesting a direct role in catalysis. Thus, although the identity of Tyr-190 is not conserved between the pseudoaglycone deacetylases and MshB (Maynes

et al., 2003; McCarthy et al., 2004), structural analysis identifies equivalent tyrosine residues at similar locations.

Functional Similarity to Other Zinc-Dependent Deacetylases

The pseudoaglycone deacetylases share notable mechanistic similarities with a number of distinct zinc-dependent deacetylases, despite the lack of any appreciable sequence similarity and topologically distinct three-dimensional structures. Each of these enzymes uses a near-identical constellation of active-site residues to carry out deacetylation of a substrate that contains an *N*-acetylglucosamine moiety. In particular, the zinc-dependent UDP-(3-O-(R-3-hydroxymyristoyl))-*N*-acetylglucosamine deacetylase LpxC (Hernick et al., 2005; McClerren et al., 2005; Whittington et al., 2003), the CE-4 family peptidoglycan deacetylase from *S. pneumoniae* (Blair et al., 2005), and the pseudoaglycone deacetylases all contain the following features: (1) an active-site pentacoordinate zinc ion that is (2) flanked by a highly conserved aspartic acid that participates in acid/base chemistry, and (3) a histidine, stabilized in the imidazolium form by an aspartic acid, which participates in electrostatic stabilization of the oxyanion of the tetrahedral intermediate. In addition, the peptidoglycan deacetylases (Blair et al., 2005), MshB (Maynes et al., 2003; McCarthy et al., 2004), and the pseudoaglycone deacetylases each contain a tyrosine residue that flanks the histidine imidazolium and is poised to further serve in electrostatic stabilization of the tetrahedral intermediate. In this subset of zinc-dependent deacetylases, an arginine residue orients and polarizes the carboxylate side chain of the aspartic acid catalytic base. The overall conservation of active-site features among these enzymes, in spite of their structurally distinct topologies, suggests that these zinc-dependent deacetylases are the product of convergent evolution.

It is interesting to note that the crystal structure of zinc-inhibited LpxC reveals a saturated fatty acid molecule, interpreted as myristic acid, in a hydrophobic tunnel adjacent to the zinc ion (Whittington et al., 2003). The fatty acid hydrocarbons in the Orf2*-decanoic acid binary complex similarly occupy a hydrophobic site near the zinc. However, in contrast to the myristate in the LpxC structure, which does not bind to the native zinc ion (Whittington et al., 2003), one of the carbonyls of the decanoic acid carboxylate coordinates directly to the zinc in Orf2*.

A Unique Capping Loop Implicated in Substrate Binding

Although the pseudoaglycone deacetylases share some topological similarities with MshB, a notable distinction is the insertion of a large loop region (residues Asp-97 through Ser-128) in Orf2* and Dbv21 (Figure 3A). This surface-exposed loop covers the active site, and is situated on the opposing end of the hydrophobic, fatty acid binding pocket. The polypeptide chain in the loop region in the Orf2* structure is mobile, as evidenced by the higher average thermal (B) factors for residues within this loop compared to those for the rest of the protein. Moreover, this loop is not observed in the structure of Dbv21, indicating significant disorder of this region in this structure (Figure 3B). Given that this loop is present only in the amino acid sequences of the pseudoaglycone deacetylases, and is located atop the active-site cavity, it is likely that the loop may be a determinant for interactions with the pseudoaglycone substrate. In order to test this hypothesis, we examined the integrity of Orf2* with limited proteolysis, in the absence and presence of substrate, with the nonspecific protease chymotrypsin.

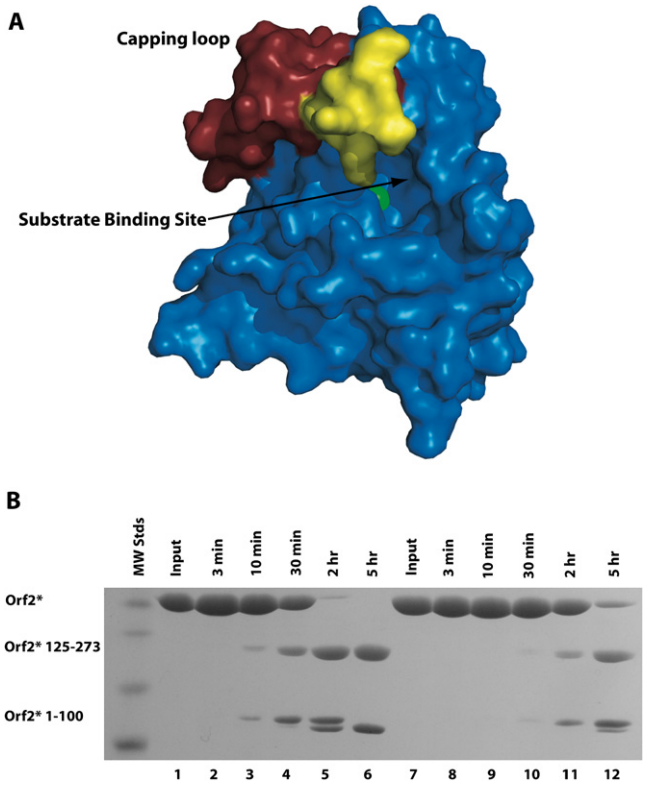

Figure 7. Possible Role for the Capping Loop in Interactions with Substrate

(A) Surface representation of the structure of Orf2* illustrating the proximity of the capping loop to the active site. The capping loop spanning residues Arg-101 through His-124 is shown in red, and residues Val-113 through Gln-117, located at the tip of the loop, are shown in yellow. The zinc ion is shown as a green sphere.

(B) Protease accessibility of the capping loop in the presence and absence of substrate. Purified recombinant Orf2* was incubated with sequencing-grade chymotrypsin at a ratio of 500:1 (enzyme:protease) in the presence (lanes 2–6) and absence (lanes 8–12) of teicoplanin, and equal volumes of the reaction were quenched at the designated time points. Addition of the substrate affords significant protection of the capping loop, suggesting that this loop is sequestered by the binding of substrate.

A time-course analysis of digestion pattern with substoichiometric quantities of chymotrypsin (1:500 ratio of protease:Orf2*) reveals that full-length Orf2* is rapidly cleaved into two fragments (Figure 7B). Mass spectrometric analysis of the fragments shows that cleavage takes place between residues Tyr-100-Arg-101 and His-124-Ser-125, located at the two ends of the active-site capping loop. Incubation of Orf2* with an excess of substrate teicoplanin prior to proteolysis affords significant protection of polypeptide, suggesting that this capping loop is sequestered upon substrate binding. The amino acid sequences for Orf2* and Dbv21 share 65% identity, but show lower sequence similarities between residues encoded in the capping loop. If the capping loop does indeed interact with the substrate, this divergence may be a consequence of having to accommodate the minor difference in the chemical structures between

N-acetyl-D-glucosaminyl teicoplanin A3-2 pseudoaglycone and *N*-acetyl-D-glucosaminyl A40926 pseudoaglycone. Additional insights into any potential roles of the capping loop in modulation substrate specificity are limited by the fact that the capping loop is disordered in the Dbv21 structure. Further investigation, such as altering the capping loops between Orf2* and Dbv21, is necessary to determine whether substrate specificity can be swapped by altering the identity of the capping loop.

Homologs of the pseudoaglycone deacetylases can also be found in gene clusters for natural products that do not contain a derivatized glucosaminyl moiety. For example, the gene clusters for the biosynthesis of balhimycin (*Amycolatopsis balhimycina* DSM 5908) (Pelzer et al., 1999) and chloroeremomycin (*Amycolatopsis orientalis* NRRL 18098) (van Wageningen et al., 1998) contain ORFs that encode for polypeptides with 60% sequence identity to the pseudoaglycone deacetylases. However, neither of these natural products contains a glucosaminyl group, and the polypeptide from the chloroeremomycin cluster is demonstrated to have thymidyltransferase activity (Ho et al., 2006). A multiple-sequence alignment of these ORFs with the pseudoaglycone deacetylases shows significant conservation throughout the entire length of the polypeptide, except for the residues in the capping loop (Figure 3C). Hence, it seems that these highly similar polypeptides have been adapted to carry out entirely different enzymatic chemistry by alteration of the residues in the active-site capping loop that is likely involved in substrate engagement.

SIGNIFICANCE

The efficacy of lipoglycopeptide antibiotics against life-threatening infections caused by Gram-positive multidrug-resistant bacteria is attributed, in part, to their characteristic *N*-acyl-D-glucosamine group. Biosynthetic approaches toward the production of lipoglycopeptides with novel acyl substituents have received significant interest as avenues for the development of new antibiotics. The elucidation of the biosynthetic routes for lipoglycopeptide production has established that *N*-acetyl-D-glucosamine is attached to the aglycone, and must be deacetylated prior to addition of the acyl group. The crystal structures of the teicoplanin and A40926 pseudoaglycone deacetylases presented here establish these enzymes as zinc-dependent deacetylases, and provide insights into the molecular basis of substrate recognition and metallo-inhibition. Despite the lack of any structural homology, these enzymes use a similar subset of active-site residues to that of the zinc-dependent deacetylases LpxC, and peptidoglycan deacetylase, suggesting that they are the products of convergent evolution. A unique capping loop shown in these structures is suggested to harbor determinants of substrate specificity, and novel specificities may likely be engineered by altering this loop. These structural results will likely further rational redesign efforts aimed toward the semisynthetic production of novel lipoglycopeptide derivatives.

EXPERIMENTAL PROCEDURES

Cloning, Protein Expression, and Purification

Bacterial strains were purchased from the American Tissue Culture Collection and the full-length cDNA fragments encoding the two pseudoaglycone deacetylases, Dbv21 and Orf2*, were amplified by polymerase chain reaction and primers based on the published sequences. The sequence of forward primer for Dbv21 was 5′-**CACC**CTGGAAGTTCTGTTCCAGGGGCCCATGTTGCAGGACGCCGACCGAACCCGG-3′ with the TOPO vector cloning site (shown in bold letters) and a Precision Protease cleavage site (shown in underlined letters) preceding the starting codon. The sequence of reverse primer for Dbv21 was 5′-CTAGCTCGAG**TTA**CTCGGCTGCGTAGCGAATGAC-3′, with the engineered stop codon TAA. The sequence of forward primer for Orf2* was 5′-**CACC**CTGGAAGTTCTGTTCCAGGGGCCCATGCCTCACGACCCCGGTGCAACC-3′, also with the TOPO vector cloning site (shown in bold letters) and Precision Protease digestion site (shown in underlined letters) preceding the starting codon. The sequence of reverse primer for Orf2* was 5′-CTAGCTCGAG**TCA**GCTGTCGTCGCTGCGGACGAC-3′, with the engineered stop codon TGA. Bacterial overexpression constructs for each Dbv21 and Orf2* were created, with amino terminal polyhistidine affinity tags, with the TOPO cloning system (Invitrogen).

The overexpression plasmids were individually transformed into *Escherichia coli* strain BL21^{star} and selected on LB-agar plates containing 50 μg kanamycin ml^{-1}. Individual colonies were diluted into 5 ml of LB containing the antibiotic, grown for 5 hr at 37°C, and then used to inoculate 1 l of LB medium containing 50 μg kanamycin ml^{-1}. Following growth at 37°C until the optical density at 600 nm reached 0.5, protein production was induced with the addition of 0.5 mM isopropyl-α-D-thiogalactopyranoside, and the cells were further grown overnight at 18°C. Bacterial cells were pelleted by centrifugation (4000 × g for 30 min) and resuspended in 100 mM KCl, 20 mM Tris-HCl (pH 8.3), and 10% glycerol. The resuspended cells were disrupted by multiple passes through an Avestin C5 Emulsiflex French press cell, and insoluble aggregates and cellular debris were removed by centrifugation (15,000 × g for 1 hr).

Recombinant Dbv21 or Orf2* was purified from the above-clarified supernatant by virtue of the amino terminal polyhistidine tag with a Talon resin (Clontech) column charged with nickel sulfate. Following elution from the nickel affinity resin, the polyhistidine tag was removed with Precision Protease (final concentration 1 μg/ml). The protein was further purified by anion exchange (5 ml HiTrap Q; G.E. Healthcare) and size-exclusion chromatography (Superdex 75 16/60; G.E. Healthcare) prior to crystallization. Selenomethionine incorporated Orf2* was produced by the method of van Duyne et al. (1993) and purified in the same manner as described above. The purity of the protein sample was greater than 95%, as judged by SDS-PAGE.

Crystallization

Crystals of both Dbv21 and Orf2* were grown by the hanging drop vapor diffusion method. For crystallization of Dbv21, 1.5 μl protein (10 mg/ml) was mixed with 1.5 μl precipitant solution containing 0.2 M magnesium acetate, 0.1 M sodium cacodylate (pH 6.5), and 12% polyethylene glycol 12,000. The mixture drop was equilibrated over a well containing the same precipitant solution at 8°C, and crystals reached their maximum size after 3 days. For crystallization of Orf2*, 1.3 μl protein (18 mg/ml) was mixed with precipitant solution containing 0.17 M sodium acetate, 0.085 M sodium cacodylate (pH 6.5), 18% polyethylene glycol 8,000, and 15% glycerol. The mixture was equilibrated over a well containing the same precipitant solution at 8°C, and crystals reached their maximum size after 5 days. Selenomethionine-incorporated Orf2* was crystallized under the same conditions, except the protein concentration was decreased to 12 mg/ml. Cocrystals of Orf2*-decanoic acid and Orf2*-octanoic acid were grown under conditions similar to that of the unliganded protein, but with the inclusion of with 10 mM ligand in the crystallization drop. In order to obtain crystals of zinc-inhibited Orf2*, crystals were soaked overnight in precipitant solution containing 10 mM zinc chloride. Crystals of Dbv21 were step-wise equilibrated with incremental concentrations of ethylene glycol up to a final concentration of 30% prior to vitrification in liquid nitrogen. All crystals of Orf2* were grown under conditions suitable for cryopreservation, and were vitrified by direct immersion into liquid nitrogen.

Phasing and Structure Determination

A four-fold redundant data set was collected from crystals of selenomethionine-substituted Orf2* at the selenium absorption edge, to a limiting resolution of 1.6 Å (overall R_{merge} = 4.3; I/σ(I) = 4.8 in the highest-resolution shell) utilizing a Mar 300 CCD detector (LS-CAT, Sector 21 ID-D; Advanced Photon Source, Argonne, IL). The structure of Orf2* was solved by single-wavelength

anomalous diffraction utilizing anomalous scattering from the three selenium-substituted methionine residues and one zinc ion per monomer. Data were indexed and scaled with the HKL2000 package (Otwinowski et al., 2003). Selenium sites were identified with the program, HySS, and the heavy atom substructure was imported to SHARP for maximum likelihood refinement and phase calculation (Bricogne et al., 2003), yielding an initial figure of merit of 0.37 to 1.77 Å resolution. Solvent flattening and phase extension to 1.6 Å resolution with the program, DM, further improved the quality of the initial map (figure of merit = 0.90) and permitted most of the main chain and 75% of the side chain residues to be automatically built with ARP/wARP (Perrakis et al., 1997). Crossvalidation used 5% of the data in the calculation of the free R factor (Kleywegt and Brunger, 1996). The remainder of the model was fitted with XtalView (McRee, 1999) and further improved by rounds of refinement with REFMAC5 (Murshudov et al., 1997, 1999) and manual building.

In order to confirm the identity of the bound metal, an X-ray fluorescence scan was conducted on crystals of native Orf2* at wavelengths near the absorption edge for zinc (LS-CAT, Sector 21 ID-D; Advanced Photon Source). The scan yielded an absorption spectrum characteristic of zinc, and a full 360° of data were collected at the peak energy level at a wavelength corresponding to the *K* absorption edge for zinc (λ = 1.2782 Å). Anomalous difference Fourier maps calculated with Bijvoet amplitudes from this data set and phases from the final refined model of Orf2*, minus the zinc atom, reveal a significant peak (> 8σ) at a position corresponding to the zinc.

The structure of native Dbv21 was determined to 2.1 Å resolution by molecular replacement (McCoy, 2007) with the refined coordinates of the SeMet Orf2* structure as a search probe. Multiple rounds of manual model building with XtalView (McRee, 1999) were interspersed with refinement with REFMAC5 (Murshudov et al., 1997, 1999) to complete structure refinement. Despite extensive manual rebuilding and refinement, residues in the capping loop region, bridging Arg-101 through Ala-125, remain ill defined and have not been modeled in the structure. As a consequence of the mobility of the residues in the capping loop, their contribution to scattering is minimal, as reflected by the fact that the free R factor of 25% for this structure is within the range of expectations for a 2.1 Å resolution structure.

The cocrystal structures of zinc inhibited Orf2* and the Orf2*-decanoic acid complex were also determined, each to 2.0 Å resolution, by molecular replacement with the refined coordinates of the SeMet Orf2* structure as a search probe, and refined by the procedures detailed above. Crossvalidation was routinely used throughout the course of model building, as was refinement with 5% of the data in the calculation of the free R factor (Kleywegt and Brunger, 1996). For each of the structures, stereochemistry of the model was monitored throughout the course of refinement with PROCHECK (Laskowski et al., 1996).

Limited Proteolysis

Orf2* was purified and the polyhistidine affinity tag was removed, as detailed above. Protein samples, at a concentration of 1 mg/ml as determined by the Bradford method, were incubated with a substoichiometric concentration of chymotrypsin (enzyme to protease ratio of 500:1) in the presence or absence of 5-fold excess of purified teicoplanin. At the defined time intervals, an aliquot of the reaction (20 μl) was mixed with an equal volume of sample buffer containing 2% SDS and incubated at 95°C in order to inactivate the protease. After completion of all of the digests, 15 μl of the quenched reaction at each time interval was resolved on a 12% Tris-SDS polyacrylamide gel. The resultant digestion pattern was visualized by staining with Coomassie blue.

ACCESSION NUMBERS

Coordinates have been deposited in the Protein Data Bank with accession codes 3DFF (Orf2*), 3DFM (Orf2*-zinc inhibited form), 3DFK (Orf2*-decanoate complex), and 3DFI (Dbv21).

ACKNOWLEDGMENTS

We thank Brian Bae and Houjin Zhang for assistance with data collection, and John Chrzas and staff at South East Regional Collaborative Access Team (22-BM at Argonne National Labs, Advanced Photon Source) for facilitating data collection. We also thank D.W. Christianson for a critical reading of the manuscript.

Received: February 4, 2008
Revised: May 2, 2008
Accepted: May 5, 2008
Published: June 20, 2008

REFERENCES

Allen, N.E., and Nicas, T.I. (2003). Mechanism of action of oritavancin and related glycopeptide antibiotics. FEMS Microbiol. Rev. *26*, 511–532.

Anstead, G.M., and Owens, A.D. (2004). Recent advances in the treatment of infections due to resistant *Staphylococcus aureus*. Curr. Opin. Infect. Dis. *17*, 549–555.

Anstead, G.M., Quinones-Nazario, G., and Lewis, J.S., II. (2007). Treatment of infections caused by resistant *Staphylococcus aureus*. Methods Mol. Biol. *391*, 227–258.

Beauregard, D.A., Williams, D.H., Gwynn, M.N., and Knowles, D.J. (1995). Dimerization and membrane anchors in extracellular targeting of vancomycin group antibiotics. Antimicrob. Agents Chemother. *39*, 781–785.

Berman, H.M., Westbrook, J., Feng, Z., Gilliland, G., Bhat, T.N., Weissig, H., Shindyalov, I.N., and Bourne, P.E. (2000). The Protein Data Bank. Nucleic Acids Res. *28*, 235–242.

Blair, D.E., Schuttelkopf, A.W., MacRae, J.I., and van Aalten, D.M. (2005). Structure and metal-dependent mechanism of peptidoglycan deacetylase, a streptococcal virulence factor. Proc. Natl. Acad. Sci. USA *102*, 15429–15434.

Bricogne, G., Vonrhein, C., Flensburg, C., Schiltz, M., and Paciorek, W. (2003). Generation, representation and flow of phase information in structure determination: recent developments in and around SHARP 2.0. Acta Crystallogr. D Biol. Crystallogr. *59*, 2023–2030.

Christianson, D.W. (1991). Structural biology of zinc. Adv. Protein Chem. *42*, 281–355.

Coggins, B.E., McClerren, A.L., Jiang, L., Li, X., Rudolph, J., Hindsgaul, O., Raetz, C.R., and Zhou, P. (2005). Refined solution structure of the LpxC-TU-514 complex and pKa analysis of an active site histidine: insights into the mechanism and inhibitor design. Biochemistry *44*, 1114–1126.

Cooper, M.A., and Williams, D.H. (1999). Binding of glycopeptide antibiotics to a model of a vancomycin-resistant bacterium. Chem. Biol. *6*, 891–899.

Cunha, B.A. (2006). Antimicrobial therapy of multidrug-resistant *Streptococcus pneumoniae*, vancomycin-resistant enterococci, and methicillin-resistant *Staphylococcus aureus*. Med. Clin. North Am. *90*, 1165–1182.

Djinovic, K., Gatti, G., Coda, A., Antolini, L., Pelosi, G., Desideri, A., Falconi, M., Marmocchi, F., Rotilio, G., and Bolognesi, M. (1992). Crystal structure of yeast Cu,Zn superoxide dismutase. Crystallographic refinement at 2.5 Å resolution. J. Mol. Biol. *225*, 791–809.

Donadio, S., Sosio, M., Stegmann, E., Weber, T., and Wohlleben, W. (2005). Comparative analysis and insights into the evolution of gene clusters for glycopeptide antibiotic biosynthesis. Mol. Genet. Genomics *274*, 40–50.

Dong, S.D., Oberthur, M., Losey, H.C., Anderson, J.W., Eggert, U.S., Peczuh, M.W., Walsh, C.T., and Kahne, D. (2002). The structural basis for induction of VanB resistance. J. Am. Chem. Soc. *124*, 9064–9065.

Gennadios, H.A., Whittington, D.A., Li, X., Fierke, C.A., and Christianson, D.W. (2006). Mechanistic inferences from the binding of ligands to LpxC, a metal-dependent deacetylase. Biochemistry *45*, 7940–7948.

Goldstein, B.P., Selva, E., Gastaldo, L., Berti, M., Pallanza, R., Ripamonti, F., Ferrari, P., Denaro, M., Arioli, V., and Cassani, G. (1987). A40926, a new glycopeptide antibiotic with anti-*Neisseria* activity. Antimicrob. Agents Chemother. *31*, 1961–1966.

Gomez-Ortiz, M., Gomis-Ruth, F.X., Huber, R., and Aviles, F.X. (1997). Inhibition of carboxypeptidase A by excess zinc: analysis of the structural determinants by X-ray crystallography. FEBS Lett. *400*, 336–340.

Hermoso, J.A., Lagartera, L., Gonzalez, A., Stelter, M., Garcia, P., Matinez-Ripoll, M., Garcia, J.L., and Menendez, M. (2005). Insights into pneumococcal pathogenesis from the crystal structure of the modular teichoic acid phosphorylcholine esterase Pce. Nat. Struct. Mol. Biol. *12*, 533–538.

 ©2008 Elsevier Ltd All rights reserved

Hernick, M., Gennadios, H.A., Whittington, D.A., Rusche, K.M., Christianson, D.W., and Fierke, C.A. (2005). UDP-3-O-((R)-3-hydroxymyristoyl)-N-acetylglucosamine deacetylase functions through a general acid-base catalyst pair mechanism. J. Biol. Chem. *280*, 16969–16978.

Higgins, D.L., Chang, R., Debabov, D.V., Leung, J., Wu, T., Krause, K.M., Sandvik, E., Hubbard, J.M., Kaniga, K., Schmidt, D.E., Jr., et al. (2005). Telavancin, a multifunctional lipoglycopeptide, disrupts both cell wall synthesis and cell membrane integrity in methicillin-resistant *Staphylococcus aureus*. Antimicrob. Agents Chemother. *49*, 1127–1134.

Hiramatsu, K., Hanaki, H., Ino, T., Yabuta, K., Oguri, T., and Tenover, F.C. (1997). Methicillin-resistant *Staphylococcus aureus* clinical strain with reduced vancomycin susceptibility. J. Antimicrob. Chemother. *40*, 135–136.

Ho, J.Y., Huang, Y.T., Wu, C.J., Li, Y.S., Tsai, M.D., and Li, T.L. (2006). Glycopeptide biosynthesis: Dbv21/Orf2 from dbv/tcp gene clusters are N-Ac-Glm teicoplanin pseudoaglycone deacetylases and Orf15 from cep gene cluster is a Glc-1-P thymidyltransferase. J. Am. Chem. Soc. *128*, 13694–13695.

Holland, D.R., Hausrath, A.C., Juers, D., and Matthews, B.W. (1995). Structural analysis of zinc substitutions in the active site of thermolysin. Protein Sci. *4*, 1955–1965.

Holm, L., and Sander, C. (1995). Dali: a network tool for protein structure comparison. Trends Biochem. Sci. *20*, 478–480.

Kahne, D., Leimkuhler, C., Lu, W., and Walsh, C. (2005). Glycopeptide and lipoglycopeptide antibiotics. Chem. Rev. *105*, 425–448.

Kleywegt, G.J., and Brunger, A.T. (1996). Checking your imagination: applications of the free R value. Structure *4*, 897–904.

Kruger, R.G., Lu, W., Oberthur, M., Tao, J., Kahne, D., and Walsh, C.T. (2005). Tailoring of glycopeptide scaffolds by the acyltransferases from the teicoplanin and A-40,926 biosynthetic operons. Chem. Biol. *12*, 131–140.

Laskowski, R.A., Rullmannn, J.A., MacArthur, M.W., Kaptein, R., and Thornton, J.M. (1996). AQUA and PROCHECK-NMR: programs for checking the quality of protein structures solved by NMR. J. Biomol. NMR *8*, 477–486.

Li, T.L., Huang, F., Haydock, S.F., Mironenko, T., Leadlay, P.F., and Spencer, J.B. (2004). Biosynthetic gene cluster of the glycopeptide antibiotic teicoplanin: characterization of two glycosyltransferases and the key acyltransferase. Chem. Biol. *11*, 107–119.

Liu, J., and Mushegian, A. (2003). Three monophyletic superfamilies account for the majority of the known glycosyltransferases. Protein Sci. *12*, 1418–1431.

Malabarba, A., Strazzolini, P., Depaoli, A., Landi, M., Berti, M., and Cavalleri, B. (1984). Teicoplanin, antibiotics from *Actinoplanes teichomyceticus* nov. sp. VI. Chemical degradation: physico-chemical and biological properties of acid hydrolysis products. J. Antibiot. (Tokyo) *37*, 988–999.

Martinez, J.L., Baquero, F., and Andersson, D.I. (2007). Predicting antibiotic resistance. Nat. Rev. Microbiol. *5*, 958–965.

Maynes, J.T., Garen, C., Cherney, M.M., Newton, G., Arad, D., Av-Gay, Y., Fahey, R.C., and James, M.N. (2003). The crystal structure of 1-D-myo-inosityl 2-acetamido-2-deoxy-alpha-D-glucopyranoside deacetylase (MshB) from *Mycobacterium tuberculosis* reveals a zinc hydrolase with a lactate dehydrogenase fold. J. Biol. Chem. *278*, 47166–47170.

McCarthy, A.A., Peterson, N.A., Knijff, R., and Baker, E.N. (2004). Crystal structure of MshB from *Mycobacterium tuberculosis*, a deacetylase involved in mycothiol biosynthesis. J. Mol. Biol. *335*, 1131–1141.

McClerren, A.L., Zhou, P., Guan, Z., Raetz, C.R., and Rudolph, J. (2005). Kinetic analysis of the zinc-dependent deacetylase in the lipid A biosynthetic pathway. Biochemistry *44*, 1106–1113.

McCoy, A.J. (2007). Solving structures of protein complexes by molecular replacement with Phaser. Acta Crystallogr. D Biol. Crystallogr. *63*, 32–41.

McRee, D.E. (1999). XtalView/Xfit—a versatile program for manipulating atomic coordinates and electron density. J. Struct. Biol. *125*, 156–165.

Moellering, R.C., Jr. (2006). Vancomycin: a 50-year reassessment. Clin. Infect. Dis. *42* (*Suppl 1*), S3–S4.

Murray, B.E. (2000). Vancomycin-resistant enterococcal infections. N. Engl. J. Med. *342*, 710–721.

Murshudov, G.N., Vagin, A.A., and Dodson, E.J. (1997). Refinement of macromolecular structures by the maximum-likelihood method. Acta Crystallogr. D Biol. Crystallogr. *53*, 240–255.

Murshudov, G.N., Vagin, A.A., Lebedev, A., Wilson, K.S., and Dodson, E.J. (1999). Efficient anisotropic refinement of macromolecular structures using FFT. Acta Crystallogr. D Biol. Crystallogr. *55*, 247–255.

Newton, G.L., Av-Gay, Y., and Fahey, R.C. (2000). N-Acetyl-1-D-myo-inosityl-2-amino-2-deoxy-alpha-D-glucopyranoside deacetylase (MshB) is a key enzyme in mycothiol biosynthesis. J. Bacteriol. *182*, 6958–6963.

Newton, G.L., Ko, M., Ta, P., Av-Gay, Y., and Fahey, R.C. (2006). Purification and characterization of *Mycobacterium tuberculosis* 1D-myo-inosityl-2-acetamido-2-deoxy-alpha-D-glucopyranoside deacetylase, MshB, a mycothiol biosynthetic enzyme. Protein Expr. Purif. *47*, 542–550.

Otwinowski, Z., Borek, D., Majewski, W., and Minor, W. (2003). Multiparametric scaling of diffraction intensities. Acta Crystallogr. A *59*, 228–234.

Pelzer, S., Sussmuth, R., Heckmann, D., Recktenwald, J., Huber, P., Jung, G., and Wohlleben, W. (1999). Identification and analysis of the balhimycin biosynthetic gene cluster and its use for manipulating glycopeptide biosynthesis in *Amycolatopsis mediterranei* DSM5908. Antimicrob. Agents Chemother. *43*, 1565–1573.

Perrakis, A., Sixma, T.K., Wilson, K.S., and Lamzin, V.S. (1997). wARP: improvement and extension of crystallographic phases by weighted averaging of multiple-refined dummy atomic models. Acta Crystallogr. D Biol. Crystallogr. *53*, 448–455.

Rawat, M., Kovacevic, S., Billman-Jacobe, H., and Av-Gay, Y. (2003). Inactivation of mshB, a key gene in the mycothiol biosynthesis pathway in *Mycobacterium smegmatis*. Microbiology *149*, 1341–1349.

Scheinfeld, N. (2007). Dalbavancin: a review. Drugs Today (Barc) *43*, 305–316.

Sieradzki, K., Roberts, R.B., Haber, S.W., and Tomasz, A. (1999). The development of vancomycin resistance in a patient with methicillin-resistant *Staphylococcus aureus* infection. N. Engl. J. Med. *340*, 517–523.

Sosio, M., Stinchi, S., Beltrametti, F., Lazzarini, A., and Donadio, S. (2003). The gene cluster for the biosynthesis of the glycopeptide antibiotic A40926 by *Nonomuraea* species. Chem. Biol. *10*, 541–549.

Sosio, M., Kloosterman, H., Bianchi, A., de Vreugd, P., Dijkhuizen, L., and Donadio, S. (2004). Organization of the teicoplanin gene cluster in *Actinoplanes teichomyceticus*. Microbiology *150*, 95–102.

Spencer, C.M., and Bryson, H.M. (1995). Teicoplanin. A pharmacoeconomic evaluation of its use in the treatment of Gram-positive infections. Pharmacoeconomics *7*, 357–374.

Truman, A.W., Robinson, L., and Spencer, J.B. (2006). Identification of a deacetylase involved in the maturation of teicoplanin. ChemBioChem *7*, 1670–1675.

Truman, A.W., Huang, F., Llewellyn, N.M., and Spencer, J.B. (2007). Characterization of the enzyme BtrD from *Bacillus circulans* and revision of its functional assignment in the biosynthesis of butirosin. Angew. Chem. Int. Ed. Engl. *46*, 1462–1464.

Van Bambeke, F. (2006). Glycopeptides and glycodepsipeptides in clinical development: a comparative review of their antibacterial spectrum, pharmacokinetics and clinical efficacy. Curr. Opin. Investig. Drugs *7*, 740–749.

van Duyne, G.D., Standaert, R.F., Karplus, P.A., Schreiber, S.L., and Clardy, J. (1993). Atomic structures of the human immunophilin FKBP-12 complexes with FK506 and rapamycin. J. Mol. Biol. *229*, 105–124.

van Wageningen, A.M., Kirkpatrick, P.N., Williams, D.H., Harris, B.R., Kershaw, J.K., Lennard, N.J., Jones, M., Jones, S.J., and Solenberg, P.J. (1998). Sequencing and analysis of genes involved in the biosynthesis of a vancomycin group antibiotic. Chem. Biol. *5*, 155–162.

Whittington, D.A., Rusche, K.M., Shin, H., Fierke, C.A., and Christianson, D.W. (2003). Crystal structure of LpxC, a zinc-dependent deacetylase essential for endotoxin biosynthesis. Proc. Natl. Acad. Sci. USA *100*, 8146–8150.

Wiliams, D.H., and Bardsley, B. (1999). The vancomycin group of antibiotics and the fight against resistant bacteria. Angew. Chem. Int. Ed. Engl. *38*, 1172–1193.

Zinner, S.H. (2007). Antibiotic use: present and future. New Microbiol. *30*, 321–325.